Research Article | Vol. 32, No. 21 / 7 Oct 2024 / Optics Express 37542
Optics EXPRESS

Noise sensitivity analysis of focal scanning light field imaging

HONGMEI PENG,[1,2] SIBO HUANG,[1,2] CHAO ZUO,[2] XIAOLI LIU,[1,3] AND ZEWEI CAI[1,3,*]

[1] *Key Laboratory of Optoelectronic Devices and Systems of Ministry of Education and Guangdong Province, College of Physics and Optoelectronic Engineering, Shenzhen University, Shenzhen, Guangdong 518060, China*
[2] *Smart Computational Imaging Laboratory (SCILab), School of Electronic and Optical Engineering, Nanjing University of Science and Technology, Nanjing, Jiangsu 210094, China*
[3] *Key Laboratory of Intelligent Optical Measurement and Detection of Shenzhen, College of Physics and Optoelectronic Engineering, Shenzhen University, Shenzhen, Guangdong 518060, China*
[*] *zeweilinc@foxmail.com*

Abstract: Light field imaging can simultaneously record spatial and angular information of light signals to provide various computational imaging functions. However, traditional microlens array-based light field cameras usually suffer from a trade-off between spatial and angular resolutions. In contrast, focal scanning light field imaging (FSLFI) can digitally modulate an incident light field through an image stack captured at different focal planes and then utilize the transport-of-intensity property to computationally recover the full-resolution light field. This paper presents a unified light field reconstruction algorithm framework, which involves different types of algorithms, such as back-projection reconstruction and additive/multiplicative iterative reconstruction, for FSLFI. Based on the unified algorithm framework, we systematically analyze and investigate the FSLFI performance on noise sensitivity. Light fields are reconstructed at different noise levels to quantitatively analyze the FSLFI performances with different types of algorithms. Both simulation and actual experimental results demonstrate that the noise sensitivity and reconstruction accuracy are constrained by each other for FSLFI. Back-projection reconstruction is appropriate in high-efficiency light field reconstruction, while additive/multiplicative iterative reconstruction is suitable for high-accuracy light field imaging at high/low noise levels. These conclusions can apply to any FSLFI method covered by the unified algorithm framework, in which appropriate algorithms can be selected for high-quality light field imaging and measurement according to specific application scenarios.

1. Introduction

Compared to traditional image detectors that only record two-dimensional intensity information, light field imaging, as a typical computational optical imaging modality, can simultaneously record four-dimensional (4D) spatio-angular information of light signals [1–3]. This enables many novel computational imaging functions, such as digital refocusing, viewpoint switching, depth-of-field extension, depth/three-dimensional (3D) sensing, and stereoscopic display. The commonly used light field imaging devices adopt a microlens array [4–6] or camera array [7,8] to directly sample spatio-angular information, having a difficult balance between high spatial and continuous angular samplings. In contrast, computational light field imaging using optical encoders, such as coded aperture [9–12], attenuation mask [13,14], diffuser [15,16], and graphene layers [17], or digital modulation can pre-modulate an incident light field and then implement light field reconstruction through spatio-angular sampling redundancy, overcoming the problem of spatial and angular resolution trade-off.

#539474 https://doi.org/10.1364/OE.539474
Journal © 2024 Received 15 Aug 2024; revised 15 Sep 2024; accepted 17 Sep 2024; published 2 Oct 2024

Optics EXPRESS

Focal scanning light field imaging (FSLFI), which uses light field propagation as digital modulation, is a high-resolution light field reconstruction (LFR) technology that has gradually gained increasing attention and research in recent years. By collecting an image stack from different focal planes, the transport-of-intensity property can be used to recover the full-resolution light field. In 2010, Levin et al. [18] pointed out that the energy of the image stack is mainly concentrated in a 3D subset of the 4D light field spectrum, and light field information can be retrieved by using an appropriate defocus blur kernel for deconvolution. In 2014, Park et al. [19] proposed a direct back-projection reconstruction (BPR) method similar to computed tomography for FSLFI. Subsequently, Mousnier et al. [20] and Chen et al. [21] overcame the defocus error problem of BPR by selecting the focused information in the image stack. In 2017, Liu et al. [22] proposed a filtered BPR method through light field projection modeling. However, because of the limited depth of field, the image stack corresponds to a limited focal scanning range, leading to low-accuracy BPR under the situation of data incompleteness. Recently, researchers have put forward different iterative reconstruction methods to eliminate artifacts and improve accuracy in incomplete reconstruction [22–27]. For example, Liu et al. [22] and Yin et al. [23] optimally solved the LFR inverse problem constructed by discrete refocusing. Blocker et al. [25] reconstructed light fields through a regularization optimization model of sparse low-rank tensors. Gao et al. successively proposed the Landweber method based on fast-guided filtering [26] and the alternating direction multiplier method [27] to achieve high-accuracy LFR. Currently, Le Bon et al. [28] presented an end-to-end unrolling optimization method for LFR from a few-shot image stack.

The aforementioned discussion shows that researchers have made significant achievements in studying specific BPR, deconvolution, and iterative reconstruction methods for FSLFI. However, comparing the FSLFI performance of each specific method remains challenging, and systematic analysis of FSLFI is still rare. In this work, we systematically analyzed FSLFI performance using noise sensitivity as a metric. Disturbance in the measurement environment may cause changes in the incident light field, and noise contamination is inevitable in image acquisition and signal transmission, ultimately affecting the LFR accuracy. To our knowledge, the noise sensitivity analysis of FSLFI has not been studied yet. To this end, we constructed a unified LFR algorithm framework involving multiplicative iterative reconstruction (MIR) and additive iterative reconstruction (AIR), where BPR can be treated as a special case of AIR in a single-cycle, unidirectional mode. Based on this unified reconstruction algorithm framework, we can analyze and investigate the systematic performance of FSLFI with different types of algorithms at different noise levels. Experimental results reveal a trade-off between noise sensitivity and reconstruction accuracy, and different types of LFR algorithms are suitable for particular application scenarios. These conclusions can apply to any FSLFI method the unified algorithm framework covers. Therefore, appropriate LFR algorithms can be selected for specific applications to achieve high-quality FSLFI.

2. Method

2.1. Light field parameterization

The term light field was first used to describe the radiometric properties of light rays in space [29] and was characterized by the plenoptic function with seven-dimensional parameters, including position, direction, wavelength, and time [30]. Light field with spatio-angular sampling is usually parameterized as [31,32]: $L(\mathbf{x}, \mathbf{u})$, where L denotes the radiant intensity, and $\mathbf{x} = (x, y)^{\mathrm{T}}$ and $\mathbf{u} = (u, v)^{\mathrm{T}}$ denote the spatial and angular coordinates, respectively. The captured two-dimensional intensity signal $I(\mathbf{x})$ is the light field integration along the angular dimensions, thus losing the direction and depth information. Unlike the traditional imaging modality of "what you see is what you get", the additional angular information enables light field imaging many novel computational imaging capabilities.

Optics EXPRESS

When the light field propagates to different focal planes, the spatial coordinates are jointly sheared by the angular coordinates and transmission distances. The integration of a sheared light field along the angular dimensions is an image at a specific focal plane, expressed as [33]:

$$I^{\mathrm{fp}}(\mathbf{x}) = \mathcal{P}_{\alpha}^{\mathrm{fp}}[L(\mathbf{x},\mathbf{u})] = \sum_{\mathbf{u}} L\left(\mathbf{x} + \left(1 - \frac{1}{\alpha}\right)\mathbf{u}, \mathbf{u}\right) \tag{1}$$

where α denotes the light field shear factor, which is the ratio of the transmission distances, $\mathcal{P}_{\alpha}^{\mathrm{fp}}$ denotes the light field forward propagation, i.e., the refocused image formation of the light field after forward shearing and spatial projection. Here, the scale of the spatial coordinates is ignored for simplicity of treatment, which does not affect the following analysis and investigation.

Refocused images carry different parts of light field information during light propagation. Changing the focal plane for imaging can capture an image stack, which thus not only carries the spatial and textural information of objects but also describes the light field propagation and contains rich light field structure information. FSLFI is to use this transport-of-intensity property to recover 4D light field information from the image stack. Therefore, the goal of LFR is to make the forward propagation of the reconstructed light field as close as possible to the raw image stack, which can be treated mathematically as an inverse problem as:

$$\arg\min_{L} \sum_{m} ||I_m(\mathbf{x}) - \mathcal{P}_{\alpha_m}^{\mathrm{fp}}[L(\mathbf{x},\mathbf{u})]||^2 \tag{2}$$

where $I_m(\mathbf{x}),\ m = 1, 2, \cdots, M$ is the captured image sequence. The light field information can then be recovered by optimally solving Eq. (2). The number of captured images used for light field reconstruction usually meets $M \geq 5$, and the total image residual less than a user-defined threshold can act as an optimization criterion. Besides, the focal planes corresponding to the image stack can cover the objective depth range as far as possible while the plane spacing is not strictly limited.

2.2. Unified LFR algorithm framework

In order to systematically analyze and investigate the FSLFI performance, we construct a unified LFR algorithm framework, as shown in Fig. 1(a). The unified algorithm framework consists of two main modules: image residual and light field update. The two modules are related by the light field forward and backward propagations. A refocused image can be obtained through forward propagation of the reconstructed light field and compared with the corresponding image in the image stack. The difference between the two images is the image residual. Back-propagating the image residual can obtain the light field error, which can be used to update the reconstructed light field. Figures 1(b) and 1(c) show the schematic diagrams of image residual and light field update for clear visualization, respectively. With the relation of light field forward and backward propagations, the image residuals and light field update modules constitute a cyclic operation. Repeating the cyclic operation on each image in the image stack can complete an overall update of the reconstructed light field.

By adding an external loop, the reconstructed light field can be overall updated several times, which constructs an iterative optimization architecture. Note that this algorithm architecture looks similar to those iterative algorithms for inverse problems, such as volumetric reconstruction from captured light field data [34]; however, their goals and principles may be quite different. We represent the entire iterative optimization process as:

$$\begin{aligned} L_{k,m+1}(\mathbf{x},\mathbf{u}) &= \mathcal{R}_{k,m}[I(\mathbf{x}); L(\mathbf{x},\mathbf{u})] \\ &= L_{k,m}(\mathbf{x},\mathbf{u}) *_2 \mathcal{P}_{\alpha_m}^{\mathrm{bp}}\{I_m(\mathbf{x}) *_1 \mathcal{P}_{\alpha_m}^{\mathrm{fp}}[L_{k,m}(\mathbf{x},\mathbf{u})]\} \end{aligned} \tag{3}$$

where $\mathcal{R}_{k,m}$ denotes the kth external, mth internal LFR, and cc denotes operator. Different operators correspond to different LFR algorithms. Specifically, $*_1$ and $*_2$ are related to the image

Optics EXPRESS

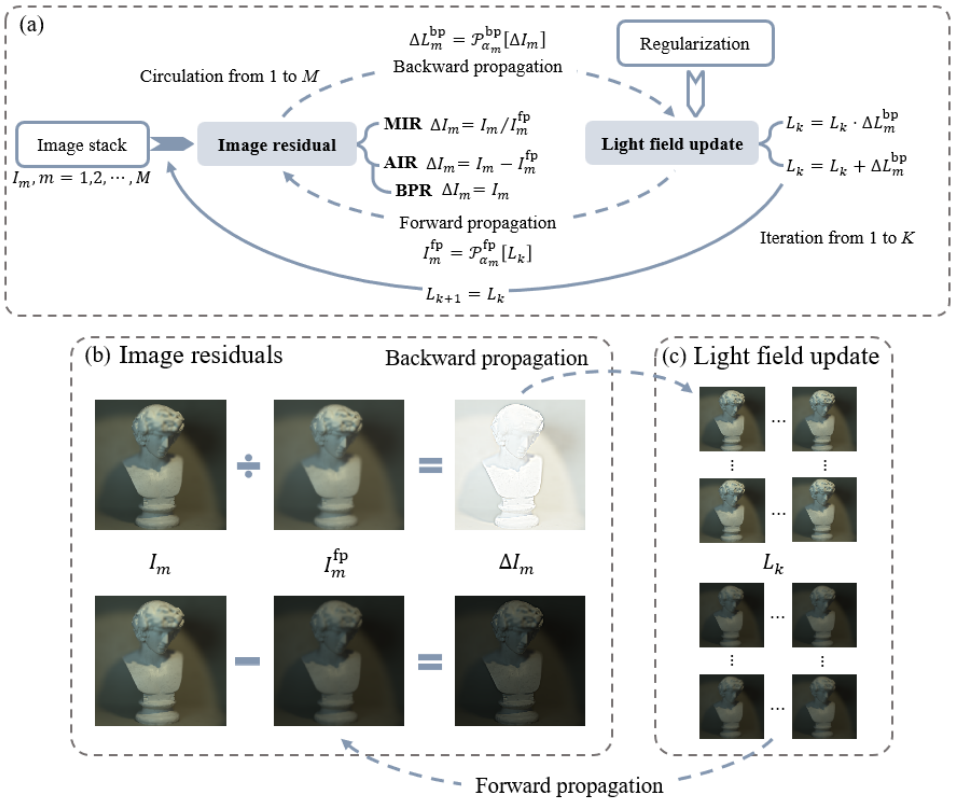

Fig. 1. Unified LFR algorithm framework: (a) iterative optimization architecture composed of image residual and light field modules, which are connected by light field forward and backward propagations; schematic diagrams of (b) image residual and (c) light field update.

residual and light field update, respectively, such that:

$$\Delta I(\mathbf{x}) = I(\mathbf{x}) *_1 I^{fp}(\mathbf{x}) \tag{4}$$

where $\Delta I(\mathbf{x})$ is the difference evaluation between the captured image $I(\mathbf{x})$ and refocused image $I^{fp}(\mathbf{x})$. $\mathcal{P}_\alpha^{bp}$ represents the light field backward propagation, where the image residual forms the light field error after angular allocation and backward shearing, expressed as:

$$\Delta L^{bp}(\mathbf{x},\mathbf{u}) = \mathcal{P}_\alpha^{bp}[\Delta I(\mathbf{x})] = \Delta I\left(\mathbf{x} - \left(1 - \frac{1}{\alpha}\right)\mathbf{u}\right) \cdot \omega(\mathbf{u}) \tag{5}$$

where $\Delta L^{bp}(\mathbf{x},\mathbf{u})$ is the light field error after backward propagation, $\omega(\mathbf{u})$ denotes angular weight factor that represents the angular allocation of the image signal. Once the mth internal iteration from 1 to M is finished, the final result of the kth external iteration is assigned to the start of the next external one, i.e., $L_{k+1,1}(\mathbf{x},\mathbf{u}) = \mathcal{R}_{k,M}[I(\mathbf{x}); L(\mathbf{x},\mathbf{u})]$.

Equation (3) is the numerical solution to the inverse problem of Eq. (2). In such iterative optimization architecture, LFR can be divided into two categories: MIR and AIR, according to the approaches of image residual calculation. MIR and AIR perform the light field update with the proportion and difference of image residuals, similar to Richardson-Lucy algorithm [35,36] and Jansson-Van Cittert algorithm [37], respectively. For MIR, $*_{1,2}$ are division and multiplication operations. In this case, the iterative optimization process related to Eq. (3) can be

Optics EXPRESS

expressed as:

$$L_{k,m+1}^{\mathrm{MIR}}(\mathbf{x},\mathbf{u}) = L_{k,m}^{\mathrm{MIR}}(\mathbf{x},\mathbf{u}) \cdot \mathcal{P}_{\alpha_m}^{\mathrm{bp}}\left\{\frac{I_m(\mathbf{x})}{\mathcal{P}_{\alpha_m}^{\mathrm{fp}}[L_{k,m}^{\mathrm{MIR}}(\mathbf{x},\mathbf{u})]}\right\} \tag{6}$$

For AIR, $*_{1,2}$ are subtraction and addition operations. Correspondently, the iterative optimization process related to Eq. (3) can be expressed as:

$$L_{k,m+1}^{\mathrm{AIR}}(\mathbf{x},\mathbf{u}) = L_{k,m}^{\mathrm{AIR}}(\mathbf{x},\mathbf{u}) + \mathcal{P}_{\alpha_m}^{\mathrm{bp}}\{I_m(\mathbf{x}) - \mathcal{P}_{\alpha_m}^{\mathrm{fp}}[L_{k,m}^{\mathrm{AIR}}(\mathbf{x},\mathbf{u})]\} \tag{7}$$

Besides, AIR has one special case. Let $k = 1$, $I_m^{\mathrm{fp}}(\mathbf{x}) = 0$, and $\omega(\mathbf{u}) = 1/M$. According to Eqs. (4) and (5), Eq. (7) can be simplified as:

$$L^{\mathrm{BPR}}(\mathbf{x},\mathbf{u}) = \frac{1}{M}\sum_m I_m\left(\mathbf{x} - \left(1 - \frac{1}{\alpha_m}\right)\mathbf{u}\right) \tag{8}$$

It is exactly the BPR method. This means that BPR is actually a special case of AIR in a single-cycle ($k = 1$), unidirectional ($I_m^{\mathrm{fp}}(\mathbf{x}) = 0$) mode. BPR only performs one overall update for the reconstructed light field without light field forward propagation in the cyclic update process. In other words, it uses the image stack to update the reconstructed light field directly.

The unified algorithm framework of FSLFI covers both non-iterative BPR and iterative LFR. Besides, FSLFI has a dimensionality gap from the image stack to the 4D light field, and the image data used for LFR is incomplete due to the limited depth of field of imaging. To reduce the impact of the dimensionality gap and data incompleteness on FSLFI performance, one can add regularization constraints to the light field update, as illustrated in Fig. 1(a).

Most FSLFI methods can be grouped into the unified LFR algorithm framework to analyze and investigate the FSLFI performance, such as comparing BPR and iterative reconstruction, the difference between AIR and MIR, and the effect of regularization constraints on LFR. Those analysis results of FSLFI performance are applicable to any FSLFI method covered by such a unified algorithm framework.

3. Experiment and analysis

In this section, we experimentally analyzed and compared the FSLFI performance on noise sensitivity based on the unified LFR algorithm framework. We employed light field data in the public HCI dataset [38] as reference light fields and captured light field images with a light field camera (Lytro) for experiments. Using the forward imaging model in Eq. (1) to compute refocused images as a simulated image stack is equivalent to using a traditional camera to capture images at different focal planes. The light field information was then retrieved from the image stack using BPR, AIR, and MIR. A maximum of 100 iterations were set for iterative reconstruction. Each iteration in AIR and MIR costs about 30 seconds, for example, in simulation experiments using a laptop (i5-12490F CPU, 32 G RAM). A threshold value (e.g., 10^{-6}) for total image residual (e.g., Frobenius norm) was set for convergence status. Finally, the noise sensitivity of different LFR algorithms was quantitatively compared and analyzed through the difference between the reconstructed and reference light fields.

3.1. Back-projection LFR

The light field data in the HCI dataset were selected for simulation experiments. The spatial and angular resolutions of the reference light field are 512×512 and 9×9, respectively. By digitally refocusing the reference light field at different focal planes, nine refocused images were obtained to form an image stack, as shown in Fig. 2(a). Digital refocusing was performed by using Eq. (1) with light field shear factors corresponding to these focal planes. Figure 2(b)

Optics EXPRESS

shows multi-view images of the reconstructed light field using BPR. The enlarged views and their respective reconstruction error maps of the margin- and center-view images marked by red, orange, and blue wireframes in Fig. 2(b) are shown in Fig. 2(c) and 2(d), respectively. The reconstructed multi-view images are blurred compared to those in the image stack. The error maps demonstrate visually larger reconstruction errors at the object edge, specifically the crown with rich texture, where many details are already indistinguishable. Table 1 lists the data of root mean square error (RMSE), structural similarity (SSIM), and peak signal-to-noise ratio (PSNR) of the reconstructed light field relative to the reference one in the margin and center views. It can be seen that the reconstruction accuracy of the center-view image is better than the margin-view one [39].

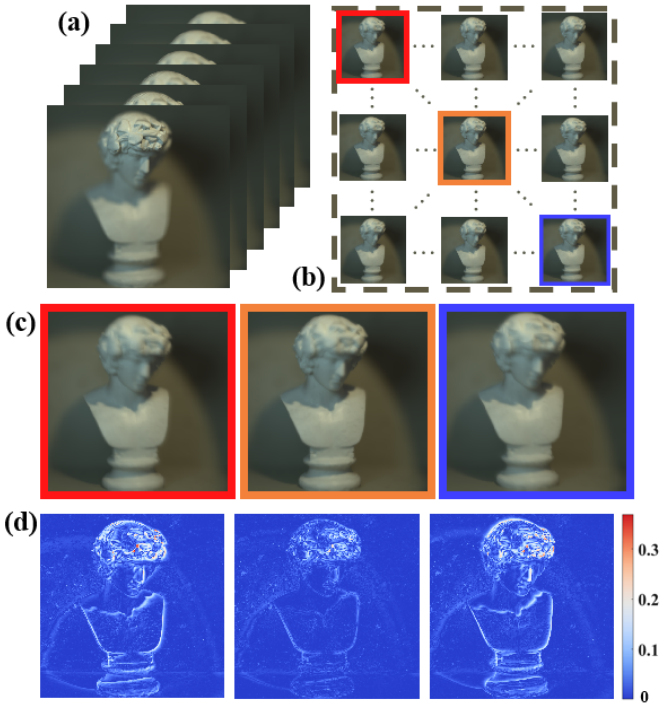

Fig. 2. BPR results: (a) image stack; (b) multi-view images of the reconstructed light field; (c) enlarged views and (d) reconstruction error maps of the margin- and center-view images marked by red, orange, and blue wireframes in (b).

Table 1. BPR errors in different views (PSNR/dB)

(u, v)	RMSE	SSIM	PSNR
(1, 1)	0.0336	0.9122	29.47
(5, 5)	0.0196	0.9377	34.17
(9, 9)	0.0341	0.9122	29.34

Next, we added zero-mean Gaussian noise to the reference light field to simulate the impact of environmental perturbation and detection noise on the FSLFI performance. The image stacks with different noise levels (controlled by the variance σ) were generated to reconstruct light fields using BPR. Figure 3(a) shows the center-view images of the reference light fields at different noise levels, along with the local enlarged views of image regions marked by the white wireframe

Optics EXPRESS

(see Visualization 1). When the noise level increases to a certain extent, the resolution of the topological structure of the object surface is affected, as shown by the third and fourth columns in Fig. 3(a). Correspondingly, the center-view images of reconstructed light fields and the corresponding error maps are shown in Fig. 3(b) and 3(c), respectively. Comparing the local enlarged views in Fig. 3(a) and 3(b), it can be seen that the BPR accuracy is not high but almost remains the same overall for different noise levels. Table 2 lists the RMSE, PSNR, and SSIM values of BPR results, showing that the BPR quality decreases slightly with increasing noise levels. Figure 3(d) plots the cross-sectional distribution curves marked by the white line in Fig. 3(c) to clearly show the details of reconstructed light fields in different views. It can be seen that BPR can obtain consistent reconstruction results at different noise levels, regardless of the margin or center views. Equation (8) demonstrates that BPR is mathematically equivalent to an average operation of the sheared image stack. This average effect enables BPR to have anti-noise ability, but at the same time, it reduces the LFR accuracy. Besides, since BPR is a special case of AIR, it indirectly indicates that AIR may also have low noise sensitivity.

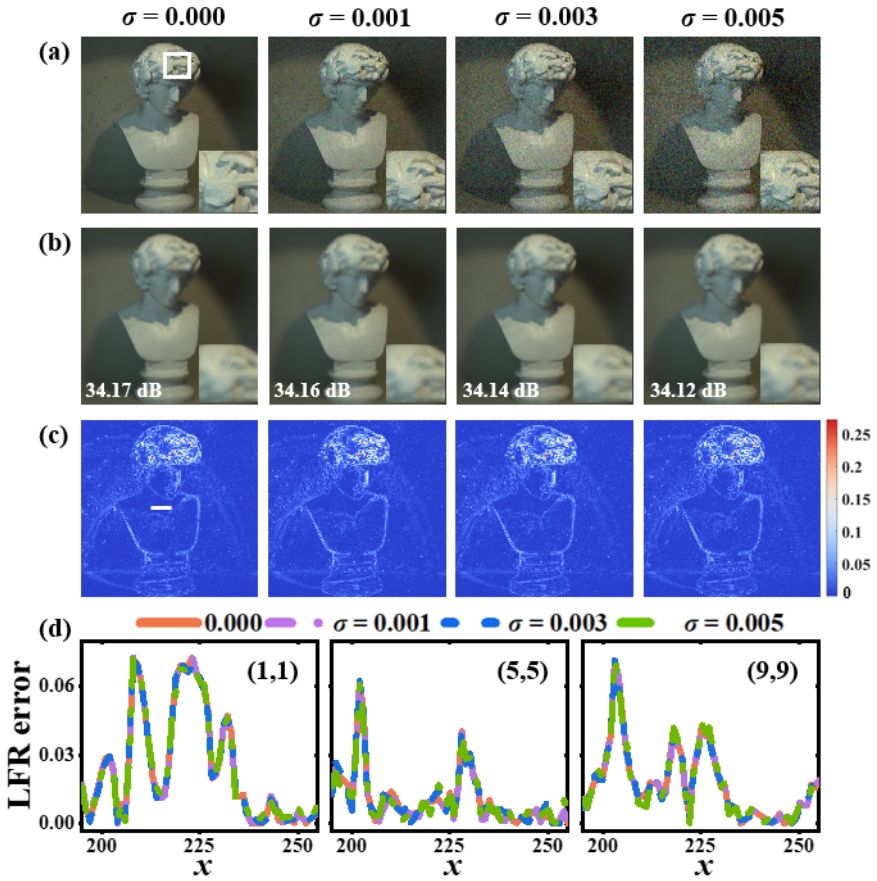

Fig. 3. BPR results at different noise levels: (a) – (b) center-view images of the reference and (b) reconstructed light fields, respectively, along with local enlarged views of image regions marked by the white wireframe; (c) reconstruction error maps corresponding to (b); (d) cross-sectional distribution curves marked by the white line in (c) in different views.

Optics EXPRESS

Table 2. LFR errors of BPR, AIR, and MIR at different noise levels (PSNR/dB)

	BPR			AIR			MIR		
σ	RMSE	SSIM	PSNR	RMSE	SSIM	PSNR	RMSE	SSIM	PSNR
0.000	0.0192	0.9377	34.17	0.0134	0.9650	37.46	0.0067	0.9804	43.48
0.001	0.0193	0.9371	34.16	0.0137	0.9566	37.23	0.0113	0.9118	38.92
0.003	0.0194	0.9359	34.14	0.0144	0.9419	36.81	0.0172	0.8035	35.29
0.005	0.0195	0.9347	34.12	0.0150	0.9290	36.47	0.0215	0.7223	33.36

3.2. *Iterative LFR*

To compare with BPR, iterative LFR was performed under the same experimental setup as in Section 3.1. Figure 4(a) shows the center-view images of reconstructed light fields using AIR and MIR at different noise levels (see Visualization 1), along with the local enlarged views of image regions marked by the white wireframe. The comparison of the local enlarged views in the first columns of Fig. 3(a), 3(b), and 4(a) reveals that in the ideal situation without noise, MIR can obtain results having fine object structure as the reference light field, thus has the highest reconstruction accuracy. Additionally, the AIR accuracy is slightly higher than BPR, so using an iterative optimization strategy in additive reconstruction can improve the LFR accuracy. On the other hand, AIR and MIR exhibited different reconstruction results with increasing noise levels. Figure 4(b) shows the reconstruction error maps corresponding to Fig. 4(a). MIR is more sensitive to noise than AIR. When the noise level increases to a certain extent, the MIR error is dominated by random noise. Figure 4(c) plots the cross-sectional distribution curves of BPR, AIR, and MIR results at different noise levels, marked the white line in Fig. 4(b). Table 2 simultaneously lists the RMSE, PSNR, and SSIM values of BPR, AIR, and MIR results for convenient comparison. Although MIR has the highest accuracy without noise, the reconstruction quality rapidly decreases with increasing noise levels. In contrast, AIR has a better noise suppression ability similar to BPR, as mentioned in Section 3.1, and the reconstruction accuracy is higher than MIR at high noise levels.

To further analyze and compare the noise sensitivity of iterative LFR, we added total variation (TV) regularization to AIR and MIR. Figure 5(a) shows the center-view images of reconstructed light fields using regularized AIR and MIR at different noise levels (see Visualization 2), along with local enlarged views of image regions marked by the white wireframe. The corresponding reconstruction error maps are shown in Fig. 5(b). Compared with Fig. 4, it can be seen that regularization constraints have a specific effect on noise suppression. In particular, regularized MIR can significantly improve the influence of noise on FSLFI. Figure 5(c) plots the cross-sectional distribution curves marked by the white line in Fig. 5(b), involving the results of AIR, MIR, and their regularized versions. Table 3 simultaneously lists the relevant data of AIR, MIR, regularized AIR, and regularized MIR results for convenient comparison. With the addition of regularization constraints, AIR obtained more consistent reconstruction results. However, the smoothing effect of TV regularization may cause reconstructed light fields to lose some object information, in turn affecting the LFR accuracy. Therefore, the noise sensitivity and reconstruction accuracy are constrained by each other for FSLFI. The accuracy of regularized MIR outperforms regularized AIR at low noise levels, but is reversed with increasing noise levels.

3.3. *Actual experiment*

Through the simulation experiments, we quantitatively compared and analyzed the noise sensitivity of FSLFI within the unified LFR algorithm framework. Here, we further verified the aforementioned analysis and discussions through actual experiments. Light field images were recorded at different noise levels by adjusting the gain and exposure time of the Lytro

Optics EXPRESS

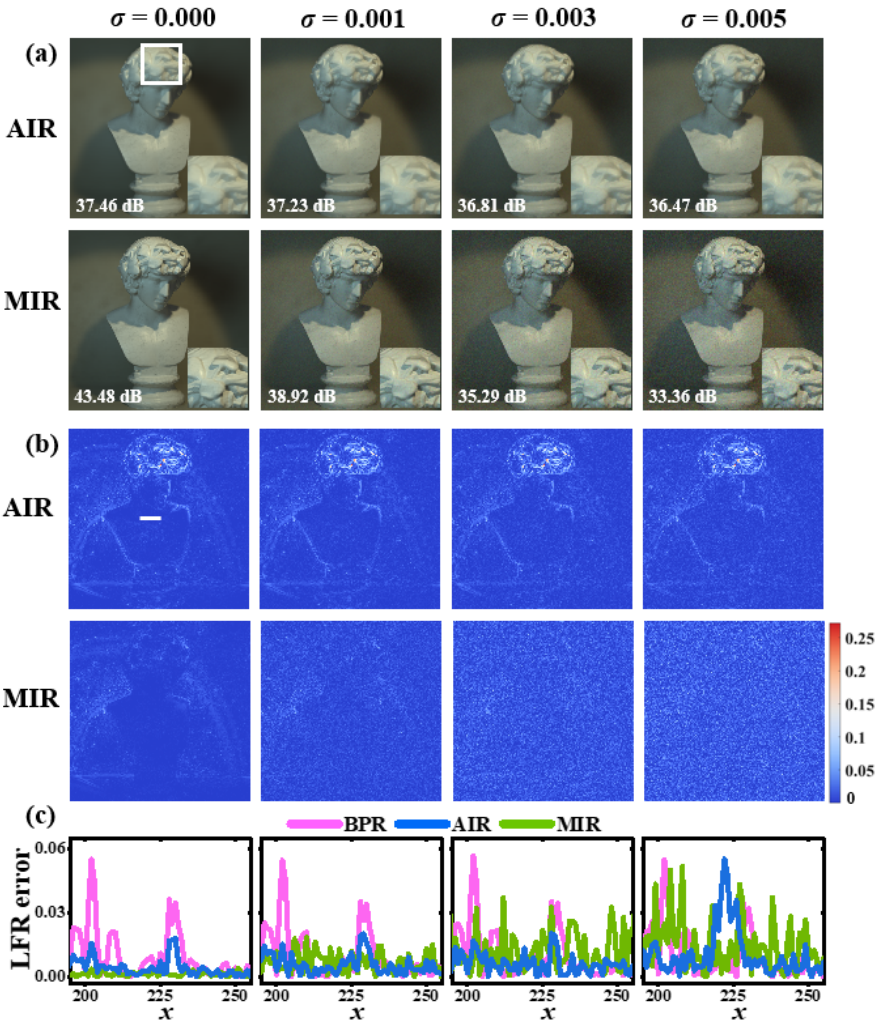

Fig. 4. AIR and MIR results at different noise levels: (a) center-view images of reconstructed light fields using AIR and MIR, along with local enlarged views of image regions marked by the white wireframe; (b) reconstruction error maps corresponding to (a); (c) cross-sectional distribution curves marked by the white line in (b).

Table 3. LFR errors of AIR, MIR, and their regularization versions at different noise levels (PSNR/dB)

	AIR			AIR+TV			MIR			MIR+TV		
σ	RMSE	SSIM	PSNR	RMSE	SSIM	PSNR	RMSE	SSIM	PSNR	RMSE	SSIM	PSNR
0.000	0.0134	0.9650	37.46	0.0148	0.9561	36.58	0.0067	0.9804	43.48	0.0103	0.9669	39.74
0.001	0.0137	0.9566	37.23	0.0149	0.9544	36.52	0.0113	0.9118	38.92	0.0127	0.9632	37.91
0.003	0.0144	0.9419	36.81	0.0152	0.9514	36.39	0.0172	0.8035	35.29	0.0146	0.9349	36.73
0.005	0.0150	0.9290	36.47	0.0153	0.9485	36.29	0.0215	0.7223	33.36	0.0193	0.8758	34.31

Optics EXPRESS

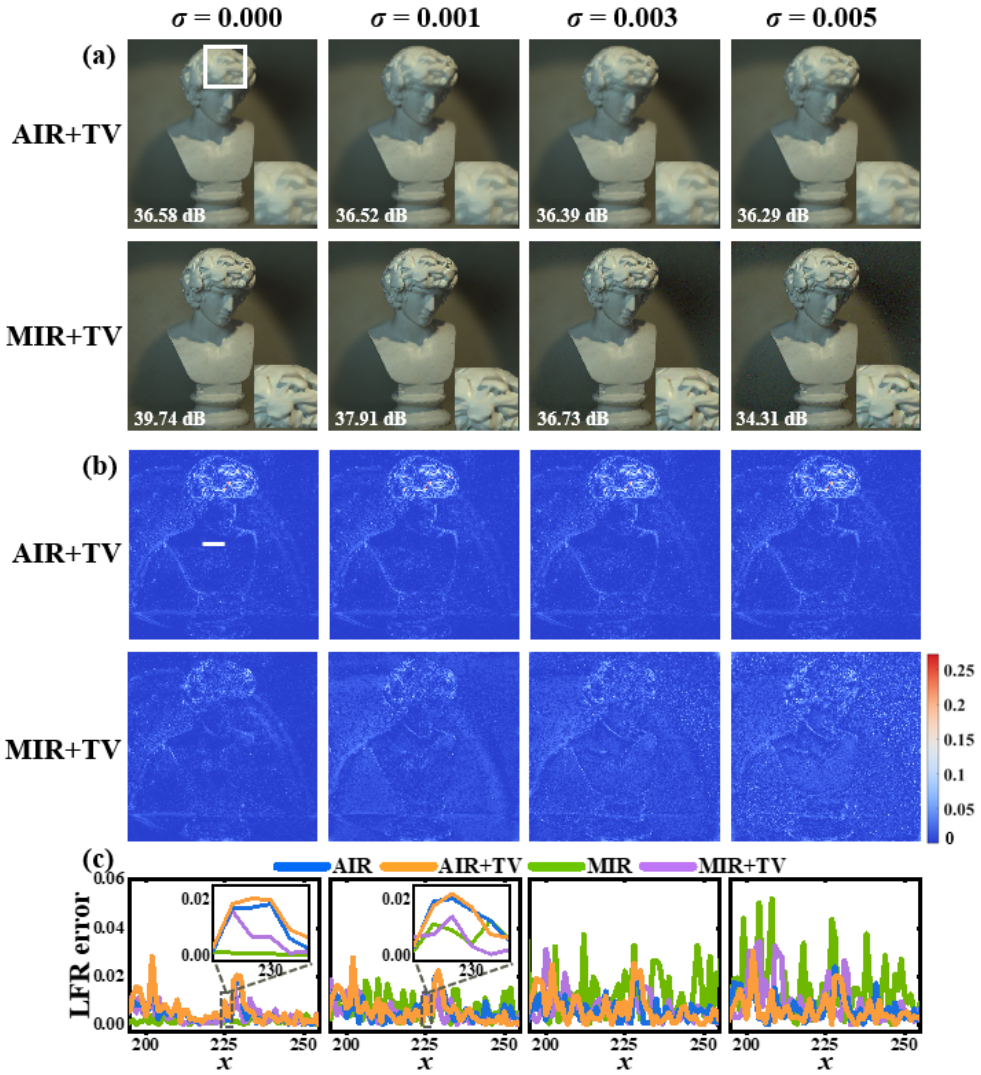

Fig. 5. Regularized AIR and MIR results at different noise levels: (a) center-view images of reconstructed light fields using regularized AIR and MIR, along with local enlarged views of image regions marked by the white wireframe; (b) reconstruction error maps corresponding to (a); (c) cross-sectional distribution curves marked by the white line in (b).

light field camera with spatial and angular resolutions of 378×379 and 11×11, respectively. Each light field image was used to generate an image stack consisting of nine refocused images to perform LFR. Figure 6 shows the center-view images of raw and reconstructed light fields using different LFR algorithms under three noise levels (increasing from left to right), along with local enlarged views of image regions marked by the red, orange, and blue wireframes. At each noise level, 20 light field images were recorded and averaged as a reference light field for comparison and analysis. Additive reconstruction (i.e., BPR and AIR) exhibited excellent noise suppression capability. In addition, the iterative optimization strategy significantly improved the LFR accuracy, and the regularization constraint further reduced the noise sensitivity with the cost of reconstruction accuracy. In comparison, MIR results had higher reconstruction accuracy to

Optics EXPRESS

retain more object details but were more noise-sensitive. It seems that regularization constraints are necessary for MIR to reduce the noise sensitivity. These results are consistent with those from simulation experiments.

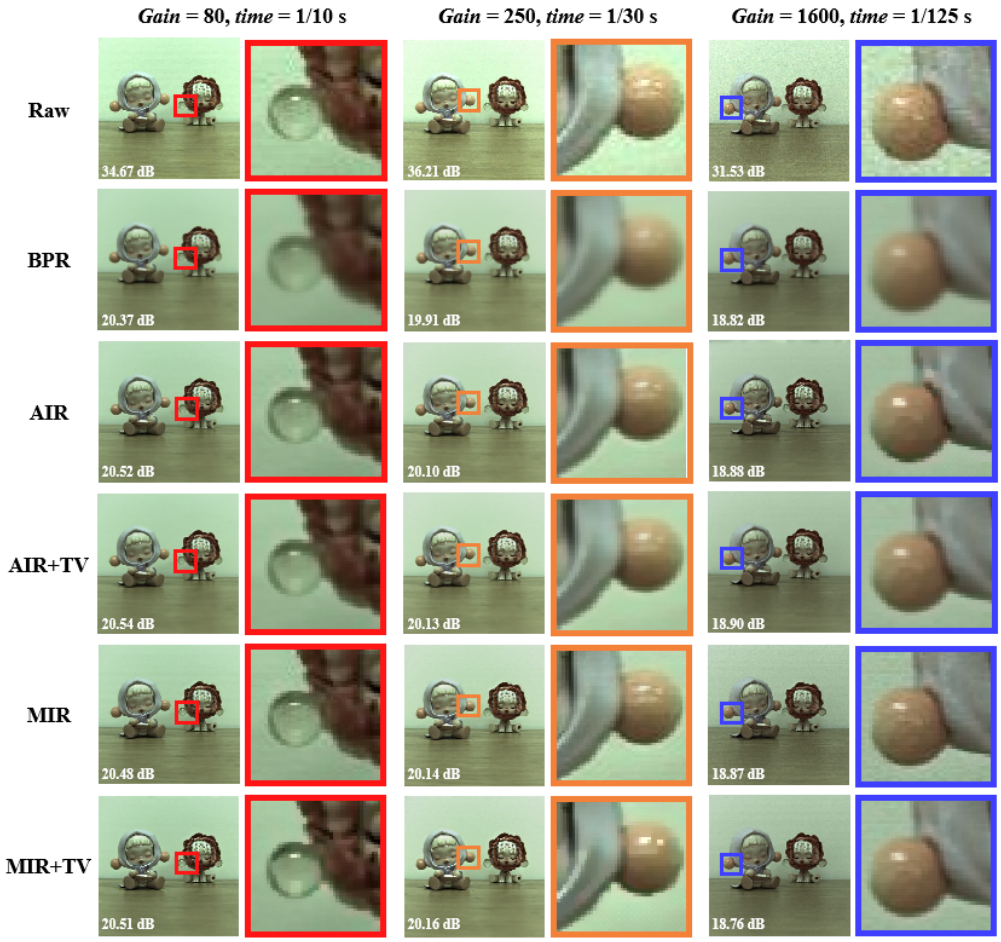

Fig. 6. Center-view images of raw and reconstructed light fields at different noise levels, along with local enlarged views of image regions marked by the red, orange, and blue wireframes.

In addition, we used the published biological light field data [40] to further expand the analysis and verification. The spatial and angular resolutions of the light field data used are 153×153 and 13×13, respectively. Similarly, FSLFI was performed using BPR, AIR, and MIR with 13 refocused images. The reconstruction results are shown in Fig. 7, along with local enlarged views of image regions marked by the white wireframe. It can be seen that all LFR algorithms demonstrate anti-noise ability for biological data, which often suffers from noise. Specifically, BPR and AIR results exhibit a certain degree of smoothness, while the MIR result has better fidelity and denoising.

Optics EXPRESS

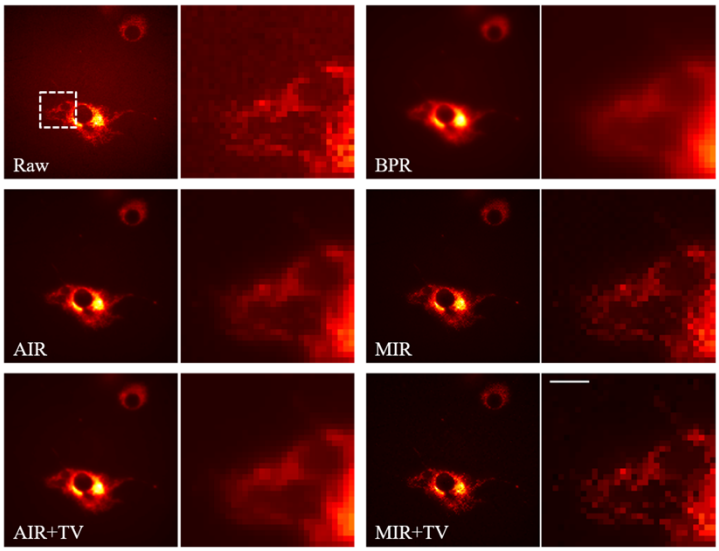

Fig. 7. Center-view images of raw and reconstructed light fields of biological data, along with local enlarged views of image regions marked by the white wireframe. Scale bar: 10 μm.

4. Discussion

The experimental results demonstrate various performances using different reconstruction algorithms and strategies. We further plotted the distribution curves of RMSE, SSIM, and PSNR values changing with the noise level for different FSLFI methods, as shown in Fig. 8. In conjunction with the experimental results, we made the following discussions:

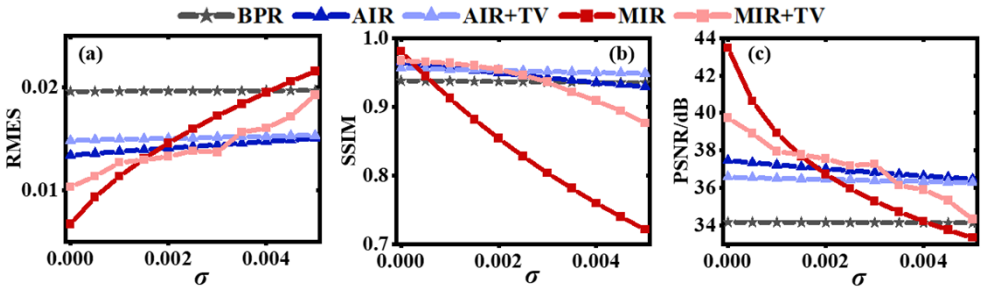

Fig. 8. Distribution curves of (a) RMSE, (b) SSIM, and (c) PSNR values changing with the noise level for different FSLFI methods.

Equation (8) used in BPR can be treated as an approximate analytical solution for retrieving 4D light field information from image stack. Such non-iterative reconstruction has a simple and efficient computational process. In particular, for high spatio-angular resolution LFR with a large depth sampling rate, iterative reconstruction becomes very time-consuming, while BPR still keeps lower computational expenses. Furthermore, the average operation of the approximate solution enables BPR to have a consistent noise suppression capability no matter the noise level. However, this in turn reduces the BPR accuracy and makes the reconstruction results blurred and so hard to restore the object information accurately. Therefore, BPR is suitable for FSLFI when relatively low accuracy but high efficiency is required.

Optics EXPRESS

Iterative reconstruction can significantly improve LFR accuracy. Specifically, AIR remains low noise sensitivity at different noise levels, similar to BPR. Besides, the addition of regularization constraints does not improve AIR performance significantly. Therefore, AIR is more balanced and suitable for FSLFI at high noise levels.

The MIR accuracy is the highest in the ideal situation without noise but decreases rapidly with increasing noise levels. In the latter case, adding the regularization constraint can significantly reduce the noise sensitivity of MIR. However, the smoothing effect of regularization will simultaneously reduce reconstruction accuracy, which is mutually constrained by noise sensitivity. Therefore, regularized MIR can be used for FSLFI at low noise levels.

Once high-resolution light fields are reconstructed by selecting appropriate LFR algorithms, high-quality imaging functions, such as fine-structure multi-view display and high-accuracy 3D sensing, can be performed. In future work, we will address the spatial inconsistency problem in FSLFI and capture actual image data for further in-depth systematic analysis to improve FSLFI performance and extend FSLFI to light field measurement applications.

5. Conclusion

In this work, we constructed a unified LFR algorithm framework based on which the FSLFI performance on noise sensitivity was investigated. Under different noise levels, the comparison of back-projection and iterative reconstructions, the difference between additive and multiplicative reconstructions, and the effect of regularization constraint on LFR were analyzed in detail. Experimental results demonstrate that different LFR algorithms are suitable for different application scenarios and are subject to the balance between noise sensitivity and reconstruction accuracy. For example, non-iterative and iterative reconstruction are suitable for high-efficiency and high-accuracy FSLFI, and additive and multiplicative reconstruction for applications with high and low noise levels, respectively. These investigations are applicable to any FSLFI method covered by the unified algorithm framework, which can be used to select appropriate LFR algorithms for high-quality FSLFI according to different application scenarios.

Funding. National Natural Science Foundation of China (62175109, 62275173, 62371311); Shenzhen Fundamental Research Program (JCYJ20220531101204010); Shenzhen Higher Education Stable Support Program (20231122025852001); Scientific Instrument Developing Project of Shenzhen University (2023YQ009); Shenzhen University Research Team Cultivation Project (2023JCT003).

Disclosures. The authors declare that there are no conflicts of interest related to this article.

Data availability. Data underlying the results presented in this paper are not publicly available at this time but maybe obtained from the authors upon reasonable request.

References

1. M. Levoy, "Light fields and computational imaging," Computer **39**(8), 46–55 (2006).
2. E. Y. Lam, "Computational photography with plenoptic camera and light field capture: tutorial," J. Opt. Soc. Am. A **32**(11), 2021–2032 (2015).
3. G. Wu, B. Masia, A. Jarabo, *et al.*, "Light field image processing: An overview," IEEE J. Sel. Top. Signal Process. **11**(7), 926–954 (2017).
4. R. Ng, M. Levoy, M. Brédif, *et al.*, "Light field photography with a hand-held plenoptic camera," Stanford Technical Report CTSR (Stanford University, 2005).
5. A. Lumsdaine and T. Georgiev, "The focused plenoptic camera," *Proc. IEEE International Conference on Computational Photography*, 1–8 (2009).
6. Y. Zhang, Y. Wang, M. Wang, *et al.*, "Multi-focus light-field microscopy for high-speed large-volume imaging," PhotoniX **3**(1), 30 (2022).
7. J. C. Yang, M. Everett, C. Buehler, *et al.*, "A real-time distributed light field camera," Proc. Thirteenth Eurographics Workshop on Rendering, 77–86 (2002).
8. B. Wilburn, N. Joshi, V. Vaish, *et al.*, "High performance imaging using large camera arrays," ACM Trans. Graph. **24**(3), 765–776 (2005).
9. A. Levin, R. Fergus, F. Durand, *et al.*, "Image and depth from a conventional camera with a coded aperture," ACM Trans. Graph. **26**(3), 70 (2007).

Optics EXPRESS

10. C.-K. Liang, T.-H. Lin, B.-Y. Wong, *et al.*, "Programmable aperture photography: multiplexed light field acquisition," Proc. ACM SIGGRAPH **27**(3), 1–10 (2008).
11. C. Zuo, J. Sun, S. Feng, *et al.*, "Programmable aperture microscopy: A computational method for multi-modal phase contrast and light field imaging," Opt. Lasers Eng **80**, 24–31 (2016).
12. Z. Cai, R. Zhang, N. Zhou, *et al.*, "Programmable aperture light-field microscopy," Laser Photonics Rev **17**(9), 2370041 (2023).
13. A. Veeraraghavan, R. Raskar, A. Agrawal, *et al.*, "Dappled photography: Mask enhanced cameras for heterodyned light fields and coded aperture refocusing," ACM Trans. Graph. **26**(3), 69 (2007).
14. K. Marwah, G. Wetzstein, Y. Bando, *et al.*, "Compressive light field photography using overcomplete dictionaries and optimized projections," ACM Trans. Graph. **32**(4), 1–12 (2013).
15. N. Antipa, S. Necula, N. Ren, *et al.*, "Single-shot diffuser-encoded light field imaging," *Proc. IEEE International Conference on Computational Photography*, 1–11 (2016).
16. Z. Cai, J. Chen, G. Pedrini, *et al.*, "Lensless light-field imaging through diffuser encoding," Light: Sci. Appl. **9**(1), 143–151 (2020).
17. M.-B. Lien, C.-H. Liu, I. Y. Chun, *et al.*, "Ranging and light field imaging with transparent photodetectors," Nat. Photonics **14**(3), 143–148 (2020).
18. A. Levin and F. Durand, "Linear view synthesis using a dimensionality gap light field prior," *Proc. IEEE Computer Society Conference on Computer Vision and Pattern Recognition*, 1831–1838 (2010).
19. J.-H. Park, S.-K. Lee, N.-Y. Jo, *et al.*, "Light ray field capture using focal plane sweeping and its optical reconstruction using 3D displays," Opt. Express **22**(21), 25444–25454 (2014).
20. A. Mousnier, E. Vural, and C. Guillemot, "Partial light field tomographic reconstruction from a fixed-camera focal stack," arXiv, (2015).
21. N. Chen, Z. Ren, D. Li, *et al.*, "Analysis of the noise in backprojection light field acquisition and its optimization," Appl. Opt. **56**(13), F20–F26 (2017).
22. C. Liu, J. Qiu, and M. Jiang, "Light field reconstruction from projection modeling of focal stack," Opt. Express **25**(10), 11377–11388 (2017).
23. X. Yin, G. Wang, W. Li, *et al.*, "Iteratively reconstructing 4D light fields from focal stacks," Appl. Opt. **55**(30), 8457–8463 (2016).
24. F. Pérez, A. Pérez, M. Rodríguez, *et al.*, "Lightfield recovery from its focal stack," J. Math. Imaging Vis **56**(3), 573–590 (2016).
25. C. J. Blocker, Y. Chun, and J. A. Fessler, "Low-rank plus sparse tensor models for light-field reconstruction from focal stack data," *Proc. IEEE 13th Image, Video, and Multidimensional Signal Processing Workshop*, 1–5 (2018).
26. S. Gao and G. Qu, "Filter-based Landweber iterative method for reconstructing the light field," IEEE Access **8**, 138340–138349 (2020).
27. S. Gao, G. Qu, M. Sjöström, *et al.*, "A TV regularisation sparse light field reconstruction model based on guided-filtering," Signal Process. Image Commun **109**, 116852 (2022).
28. B. Le Bon, M. L. Pendu, and C. Guillemot, "Joint Fourier Disparity Layers unrolling with learned view synthesis for light field reconstruction from few-shots focal stacks," IEEE Access **11**, 123350–123360 (2023).
29. A. Gershun, "The light field," J. Math. Phys. (Cambridge, Mass.) **18**(1-4), 51–151 (1939).
30. E. H. Adelson and J. R. Bergen, "The plenoptic function and the elements of early vision," in *Computational Models of Visual Processing* (MIT Press, 1991), Vol. 1, pp. 3–20.
31. M. Levoy and P. Hanrahan, "Light field rendering," *Proc. The 23rd Annual Conference on Computer Graphics and Interactive Techniques*, 31–42 (1996).
32. J. Steven, Radek Gortler, Grzeszczuk, *et al.*, "The lumigraph," *Proc. The 23rd Annual Conference on Computer Graphics and Interactive Techniques*, 43–54 (1996).
33. R. Ng, "Fourier slice photography," in ACM SIGGRAPH (2005), pp. 735–744.
34. Z. Lu, J. Wu, H. Qiao, *et al.*, "Phase-space deconvolution for light field microscopy," Opt. Express **27**(13), 18131–18145 (2019).
35. W. H. Richardson, "Bayesian-based iterative method of image restoration," J. Opt. Soc. Am. **62**(1), 55–59 (1972).
36. L. B. Lucy, "An iterative technique for the rectification of observed distributions," Astron. J **79**, 745–754 (1974).
37. R. C. Puetter, T. R. Gosnell, and A. Yahil, "Digital image reconstruction: Deblurring and denoising," Annu. Rev. Astron. Astrophys. **43**(1), 139–194 (2005).
38. S. Wanner, S. Meister, and B. Goldluecke, "Datasets and benchmarks for densely sampled 4D light fields," Proc. Vision, Modeling & Visual **13**, 225–226 (2013).
39. Y. Liu, R. Zhang, S. Feng, *et al.*, "Consistency analysis of focal stack-based light field reconstruction," Opt. Lasers Eng **165**, 107539 (2023).
40. Z. Lu, Y. Liu, M. Jin, *et al.*, "Virtual-scanning light-field microscopy for robust snapshot high-resolution volumetric imaging," Nat. Methods **20**(5), 735–746 (2023).